Dalton Transactions

Probing the Effect of Nitro-substituents in the Modulation of LUMO Energies for Directional Electron Transport through 4d6 Ruthenium(II)-based Metallosurfactants

Journal:	*Dalton Transactions*
Manuscript ID	DT-ART-06-2023-001797.R1
Article Type:	Paper
Date Submitted by the Author:	29-Jul-2023
Complete List of Authors:	Verani, Claudio; Wayne State University, Chemistry Amunugama, Samudra; Wayne State University, Chemistry Asempa, Eyram; North Carolina State University at Raleigh, Chemistry Jakubikova, Elena; North Carolina State University, Chemistry

ARTICLE

Probing the Effect of Nitro-substituents in the Modulation of LUMO Energies for Directional Electron Transport through 4d^6 Ruthenium(II)-based Metallosurfactants

Received 00th January 20xx,
Accepted 00th January 20xx

DOI: 10.1039/x0xx00000x

Samudra Amunugama,[a, †] Eyram Asempa,[b] Elena Jakubikova,[b,*] and Cláudio N. Verani [a,*]

Electron-withdrawing nitro-substituents were installed onto terpyridine- and phenanthroline-based metallosurfactants with 4d^6 ruthenium(II), which were deposited as Langmuir-Blodgett monolayers aiming to study the feasibility of charge transport in Au|LB|Au junctions. The nitro groups are intended to modulate the energy of the frontier molecular orbitals to near to, or match that of Fermi levels in the gold electrodes. A series of heteroleptic metallosurfactants [Ru^{II}(C_{18}OPh-terpy)(X-terpy)](PF_6)$_2$ and [Ru^{II}(C_{18}OPh-terpy)(X-phen)Cl]PF_6 were synthesized, where C_{18}OPh-terpy is the 4'-[4-(octadecyloxy)phenyl]-2,2':6',2''-terpyridine amphiphile common to all species, X-terpy is a terpyridine with —H **(1)** or —phenyl-NO_2 **(2)** and X-phen is a phenanthroline with —H **(3)** or —NO_2 **(4)** groups. These metallosurfactants were characterized by experimental and computational methods, and the presence of nitro groups affect more affordable reductions at less negative potentials, as well as slightly more positive oxidations, these changes are less pronounced in species **2** than in **4.** Species **1** and **2** showed limited Pockels-Langmuir and Langmuir-Blodgett film formation with lower collapse pressure of 27 mNm^{-1}. In contrast, metallosurfactants **3** and **4** showed enhanced hydrophilicity indicated by higher collapse pressures of *ca*. 36 mNm^{-1}. The LB monolayers of **3** and **4** were deposited on gold electrodes to form Au|LB|Au junctions and electron transport was measured as I/V curves. The NO_2-bearing species **4** showed asymmetric curves associated with directional electron transport with amplitudes up to -2.0 nA and rectification ratios from 5 to 26 between -1 to +1 V and from 3 to 14 between -3 to +3 V.

Introduction

Electron transport requires favorable energy matching between the electrodes and the frontier orbitals of the molecule in both single-molecule and thin film E_1|molecule|E_2 junctions.[1] Metal-terpyridine complexes have been a staple motif in such studies, and have enabled the study of bidirectional transport —observed as a sigmoidal change in current (I) while the potential (V) is varied[2]— demonstrating that the molecule acts as a wire. Park *et al.*[3] demonstrated that a high-spin 3d^7 [Co^{II}(S-terpy)$_2$] species containing thiol-substituted terpy ligands able to self-assemble into gold electrodes enable electron transport by means of the redox conversion given by ^{HS}3d^{7}Co^{II} → ^{LS}3d^{6}Co^{III} + e$^-$. The use of thiol spacers of different lengths controlled their response; while a Co species decorated with a short spacer showed a Kondo effect, or temperature-dependent electron transport, longer pentacyl spacers led to a Coulomb blockade, or increased resistance that makes the species insulating. Shortly thereafter Fan, Zhou *et al.*[4] proposed the use of acetate-substituted 3d^6 [Fe^{II}(OAc-terpy)$_2$] species in nanowire-field effect transistors for memory storage. A gating behavior similar to that of a transistor was demonstrated by van der Zant *et al.*[5] using a high spin 3d^5 [Mn^{II}(S-terpy)$_2$] species. Here reduction triggered a spin blockade or resistance due to the transition from high to low spin configuration described as $t_{2g}^3e_g^2$ + e$^-$ → $t_{2g}^6e_g^0$. The study evidences the relevance of the 3d t_{2g}-like manifold for electron transport. A seminal work by Lacroix *et al.*[6] showed that improved conductivity is observed for 3d^7 Co^{II} when compared to 4d^6 Ru^{II} in similar [M^{II}(terpy)$_2$] species. This is due to a smaller HOMO/LUMO gap that enables affordable Co^{II}/Co^{III} redox process described as $t_{2g}^6e_g^1$ → $t_{2g}^6e_g^0$ + e$^-$ and leads to LUMO conductance 250x higher than that of the 4d ion. That observation led Sachan and Mondal[7] to study potentially optoelectronic hierarchical[8] junctions such as ITO|5x(Fe/terpy)|electrolyte|5x(Co/terpy)|ITO.

Nonetheless the use of 4d metal ions such as ruthenium offer kinetic and thermodynamic advantages such as structural stability, inertness that precludes ligand dissociation, and well-behaved electrochemistry. The larger t_{2g}/e_g ligand field gap Δ_o leads to low spin configurations, and along with polypyridine ligands, the 4d^6 Ru^{II} ion is particularly attractive towards photoswitchable processes. An initial study by Yu *et al.*[9] on (dodecane-thiolate)$_2$bipyridine-Ru^{II}(acetylacetonate)$_2$ wires proposed the involvement of the metal-based HOMO, equivalent to the t_{2g} manifold in the $t_{2g}^6e_g^0$ configuration. The assignment was based on the change from a bidirectional sigmoidal I/V response for the organic dodecane-thiolate to a unidirectional rectification response attained by inclusion of the [Ru^{II}(acac)$_2$] module. A detailed study by Lee *et al.*[10]

[a] Department of Chemistry, Wayne State University, Detroit, MI 48202, USA. Email: Claudio.verani@wayne.edu
[b] Department of Chemistry, North Carolina State University, Raleigh, NC 27695, USA Email: ejakubi@ncsu.edu
† Intel corporation,Ronler Acres 4, 2501 NE Century Blvd, Hillsboro, Oregon 97124,USA Samudra.amunugama@intel.com
Electronic Supplementary Information (ESI) available: [details of any supplementary information available should be included here]. See DOI: 10.1039/x0xx00000x

using a $[Ru^{II}(S\text{-}terpy)_2]$ species proposed that electron transport must occur through the LUMO level because the HOMO is mismatched with the Fermi levels of the electrodes. Their assessment was based on Hipps[11] and Armstrong[12] models to convert electrochemical redox potentials into solid state vacuum potentials for comparison with Fermi level values. This approach is also used by us and discussed later in greater detail. The same group went on to use $[Ru^{II}(S\text{-}C_x\text{-}terpy)_2]$ species with C_7- and C_{13} lengths to attain non-volatile memory elements. A recent account by Ding, Yu *et al*. describes electron transport in terms of bipolaron transport and Pauli spin blockade that relates to the consequences of spin flip.[13]

Another seminal work by Rignanese *et al*.[14] used first-principles electronic structure calculations to confirm the mismatch between Fermi and Ru-based HOMO and to conclude that ligand involvement, rather than the inaccessible Ru-based LUMO promotes electron transfer in $Ru(terpy)_2$ species. They propose that functionalization of terpy with donor and acceptor substituents could lead to planned unidirectional transport, or rectification, characterized by asymmetric I/V curves that differ from the sigmoidal I/V response seen for the above examples. In order to attain the proposed rectifying behavior, Lacroix *et al.*[15] coupled a naphthalenediimine acceptor through a phenyl bridge to $Ru(terpy)_2$, which acts as a donor. Although the mechanism of rectification was not pursued, they seem to have built a classic $E_1|D\text{-}\pi\text{-}A|E_2$ junction in which the preferred electron flow is donor → acceptor.[1e, 16]

Our groups recently demonstrated directional transport in a heteroleptic $^{LS}4d^5$ $[Ru^{III}(C_{18}OPh\text{-}terpy)(SQ)Cl]PF_6$ metallosurfactant in which C_{18}-Ph-terpy is the amphiphilic ligand 4'-(4-octadecyloxyphenyl)-2,2':6',2''-terpyridine and SQ is the deprotonated aminosemiquinone form of the ligand 2,4-di-tert-butyl-6-(phenylamino)phenol ligand.[17] The asymmetric I/V profile of this species lies in distinct contrast with the symmetric response obtained by the other $[Ru(terpy)_2]$ species and the electronic and redox results point out to a low lying SQ-based LUMO near the Fermi level of the electrodes as responsible for electron transport. These results allowed us to hypothesize that heavily distorted O_h species with distinct N, O, and Cl donors enable transport through empty and heavily mixed molecular orbitals with predominant ligand character. Here we propose the use of strong electron-withdrawing groups attached to polypyridyl ligands terpyridine and phenanthroline to induce the lowering of empty ligand-based orbitals, thus enabling directional electron transport. In order to test this proposal, we have synthesized and characterized a series of heteroleptic metallosurfactants described as $[Ru^{II}(C_{18}OPh\text{-}terpy)(terpy)](PF_6)_2$ **(1)**, $[Ru^{II}(C_{18}OPh\text{-}terpy)(NO_2Ph\text{-}terpy)](PF_6)_2$ **(2)**, $[Ru^{II}(C_{18}OPh\text{-}terpy)(phen)Cl]PF_6$ **(3)**, and $[Ru^{II}(C_{18}OPh\text{-}terpy)(NO_2\text{-}phen)Cl]PF_6$ **(4)**. In this paper we report on the electronic, electrochemical, film formation and junction properties of these species, and discuss the role of those electron-withdrawing groups on making directional electron transport possible in 4d metallosurfactants.

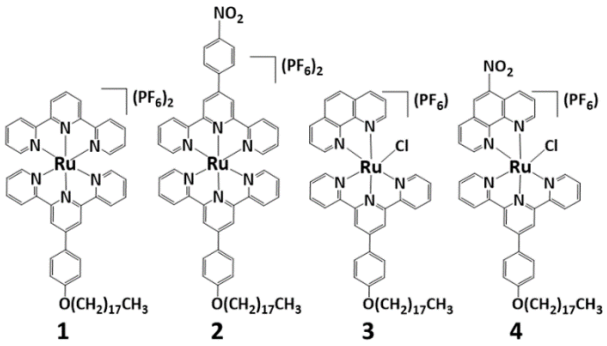

Scheme 1. Ruthenium(II) metallosurfactants **1-4.**

Results and discussion

Rationale for the molecular design

Asymmetric molecules with energetically accessible molecular orbitals are pivotal for attaining directional electron transport. Hence, we hypothesize that the incorporation of electron-withdrawing $-NO_2$ substituents will deplete electron density from the polypyridine ligand frames influencing favorably the energy of the frontier orbitals in the molecule and approaching or matching the energy associated with the Fermi levels of the electrodes. As such, directional electron transport through the molecule should be facilitated.

Synthesis and Characterization

The ligand 4'-[4-(octadecyloxy)phenyl]-2,2':6',2''-terpyridine ($C_{18}OPh$-terpy) is common to all species discussed here. This ligand and 4'-[4-(nitro)phenyl]-2,2':6',2''-terpyridine (NO_2-phen) were synthesized by a multistep process according to previously reported methods.[18] The ligands 2,2':6',2''-terpyridine (terpy), 1,10-phenanthroline (phen) and 5-nitro-1,10-phenanthroline (NO_2Ph-terpy) were obtained from commercially available sources. The heteroleptic metallosurfactants $[Ru^{II}(C_{18}OPh\text{-}terpy)(terpy)](PF_6)_2$ **(1),** $[Ru^{II}(C_{18}OPh\text{-}terpy)(NO_2Ph\text{-}terpy)](PF_6)_2$ **(2)**, $[Ru^{II}(C_{18}OPh\text{-}terpy)(phen)Cl]PF_6$ **(3)**, and $[Ru^{II}(C_{18}OPh\text{-}terpy)(NO_2\text{-}phen)Cl]PF_6$ **(4)** were synthesized in a stepwise way using $Ru(DMSO)_4Cl_2$ as the metal precursor and introducing the heteroleptic ligand sequentially. The crude products were purified by column chromatography to yield microcrystalline species characterized by ^{1}H-NMR, ^{13}C-NMR, COSY-NMR, HSQC-NMR spectroscopy, UV-visible spectroscopy, and high-resolution ESI mass spectroscopy (**Figure S1)**, where peak clusters show the expected envelope with both ruthenium (**1-4**) and chloride (**3-4**) signatures. Distinct stretching vibration peaks observed for metallosurfactants **1-4** at 2851-2923 cm^{-1} and 840-850 cm^{-1}, and respectively attributed to the $\nu_{C\text{-}H}$ modes of the ligands and the $\nu_{P\text{-}F}$ mode of the PF_6^- counterion, further validate this description.

Molecular structure

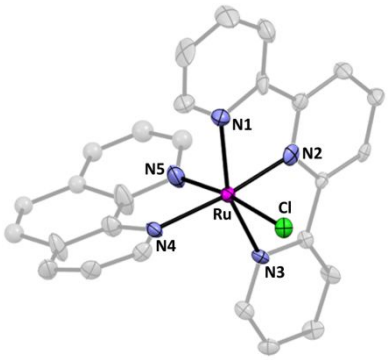

Figure 1: Connectivity of $[Ru^{II}(terpy)(phen)Cl]^+$ species.[19]

Several attempts to obtain X-ray quality crystals for **1-4** were unsuccessful, likely due to the presence of the long octadecyl chains. We considered modeling the coordination sphere experimentally by growing crystals with simpler terpyridine and phenanthroline ligands, ultimately concluding that previous literature reports suffice to describe accurately the bonding and geometry of similar compounds with $[Ru(terpy)_2]$ [20] and [Ru(terpy)(phen)] motifs.

Species with [Ru(terpy)(phen)] are available[19] in our group as the crystal structures of $[Ru^{II}(MeMPTP)(phen)Cl]^+$, $[Ru^{II}(MeMPTP)(Me_2\text{-}phen)Cl]^+$ and $[Ru^{II}(MeMPTP)(Me_4\text{-}phen)Cl]^+$ complexes (MeMPTP = 4'-(4methylmercaptophenyl)-2,2':6'2''-terpyridine), which indicate that the terpyridine, phenanthroline, and chlorido ligands enforce a pseudo-octahedral geometry around the ruthenium center (**Figure 1**).[19] The Ru-N_{terpy} bonds vary from *ca.* 1.90-2.10 Å, with the bond length between Ru and the central N2 being the shortest at 1.95 Å due to the steric effect imposed by the ligand. The Ru-N_{phen} bonds reach 2.07±0.02 Å. Additionally, Schofield *et al.*[21] reported that the biting angle between the ruthenium metal center and the outer terpyridine rings in [Ru(terpy)(phen)] species reach between 158.6-159.3°, thus deviating from the ideal 180° expected for an idealized octahedral geometry. The Ru-N_{phen} bond lengths vary according to the substituents attached to the phenanthroline ligand.[19] The average Ru-N_{phen} bond length is between 2.039-2.057 Å, where the Ru-N_{phen} bond that is trans to the Cl group is shorter compared to the bond that is trans to the central pyridine ring of the terpyridine ligand.[22]

The room-temperature 1D and 2D NMR analyses of ligands and the complexes were performed in CD_2Cl_2 and are shown in **Figure 2(a)** and **Figures S2-S8** in the supplementary information. The $terpy^{OC18}$ ligand exhibits seven peaks in the aromatic region, corresponding to fourteen H atoms, indicating the highly symmetric nature of the ligand. As expected, protons H13 and H15, as well as H6 and H31 of $terpy^{OC18}$ and $terpy^{NO2}$ ligands show a considerable degree of upfield shift compared to the free ligand due to the coplanarity of the ligand and the transoid conformation of the terminal pyridine rings compared to the central pyridine ring in the complex.[23] The ^{1}H-NMR peak resonances of $[Ru^{II}(C_{18}OPh\text{-}terpy)(terpy)](PF_6)_2$ **(1),** $[Ru^{II}(C_{18}OPh\text{-}terpy)(NO_2Ph\text{-}terpy)](PF_6)_2$ **(2),** $[Ru^{II}(C_{18}OPhterpy)(phen)Cl]PF_6$ **(3),** and $[Ru^{II}(C_{18}OPh\text{-}terpy)(NO_2\text{-}phen)Cl]PF_6$ **(4)** were assigned based on homonuclear correlation spectroscopy (COSY) and heteronuclear multiple quantum coherence (HMQC) experiments. While the aliphatic region of the ^{1}H-NMR spectrum of **1-4** is mainly comprised of signals belonging to the octadecyl chain, the aromatic regions show considerable differences. Upon coordination to the metal center, the terpy ligand adopts a cis:cis type orientation[24], and as a result, most of $terpy^{OC18}$ ligand peaks of these species show an upfield peak shift in their NMR spectrum.[25] Complexes **1** and **2** show the expected symmetric signals in the ^{1}H-NMR spectrum owing to the presence of C_{2v} ligand environments around the metal center. In compounds **3** and **4**, a significant downfield shift was observed for proton H29 of the phenanthroline, compared to its corresponding peak position in the free ligand. This peak shift can be explained considering the orthogonal arrangement of the phenanthroline ligand in the molecular structure of **3-4**, where proton H29 is shielded by the outer ring currents of the terpyridine ligand.[26] Consequently, the peak associated with proton H20 of the phenanthroline appears downfield to H29. Similarly, the peak resonances of protons H6 and H22 in terpy are shifted upfield. The electron-withdrawing nature of the -NO_2 group in **4** further influences the peak position of the adjacent proton H24 and it appears downfield to the equivalent peak in **3**.

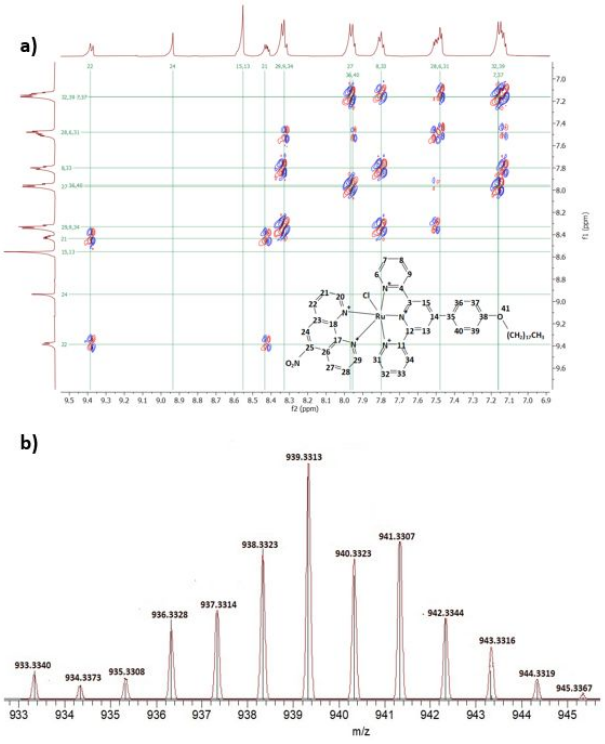

Figure 2: (a) COSY NMR Spectrum of the aromatic region of **4** in CD_2Cl_2 (b) High-resolution ESI-mass spectrum of **4** in acetonitrile

Electronic structure

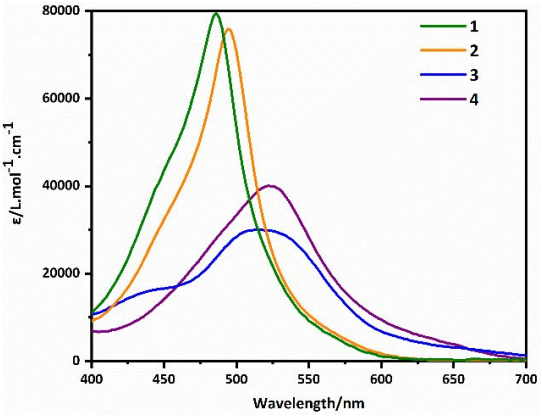

Figure 3: Visible region of the UV-visible spectrum for **1-4** in dichloromethane**.**

The electronic spectra of metallosurfactants $[Ru^{II}(C_{18}OPh\text{-}terpy)(terpy)](PF_6)_2$ **(1),** $[Ru^{II}(C_{18}OPh\text{-}terpy)(NO_2Ph\text{-}terpy)](PF_6)_2$ **(2),** $[Ru^{II}(C_{18}OPh\text{-}terpy)(phen)Cl]PF_6$ **(3)**, and $[Ru^{II}(C_{18}OPh\text{-}terpy)(NO_2\text{-}phen)Cl]PF_6$ **(4)** were recorded in 10^{-4} M dichloromethane and are shown in **Figures 3** and **S9**. All complexes show intense absorption bands in the UV region corresponding to ligand-centered charge transfer transitions. The bands between 232-244, 268-284, and 307-317 nm are intraligand processes associated with π → π* and n → π* transitions (**Figure S9**).[20c, d] The visible region of the electronic spectrum is dominated by distinct absorption bands around 485-522 nm (Δ = 37 nm) corresponding to a metal-to-ligand CT transition (MLCT) from Ru(dπ) → terpy (π*).[19, 22, 24a, 27] Because the relative stability of the t_{2g}-like molecular orbitals depends on the electron affinity of the quasi-axial ligand,[20b, 21a] species **3** and **4** contain a chlorido ligand and display a redshifted MLCT band when compared to species **1** and **2**. Additionally, **3** exhibits another CT band at 429 nm associated with a Ru(dπ) → phen(π*) transition. The absence of a similar charge transfer band in the nitro-species **4** suggests that this electronic transition is dependent on the nature of the substituents attached to the phenanthroline ligand.[19]

Electrochemical behavior

Redox potentials report on the electron density around the ruthenium center. In order to gain insight into the effect of the electron-withdrawing nitro-substituent on the energies of the frontier molecular orbitals in $[Ru^{II}(C_{18}OPh\text{-}terpy)(terpy)](PF_6)_2$ **(1),** $[Ru^{II}(C_{18}OPh\text{-}terpy)(NO_2Ph\text{-}terpy)](PF_6)_2$ **(2)**, $[Ru^{II}(C_{18}OPh\text{-}terpy)(phen)Cl]PF_6$ **(3)**, and $[Ru^{II}(C_{18}OPh\text{-}terpy)(NO_2\text{-}phen)Cl]PF_6$ **(4)**, cyclic voltammetric experiments were performed in dichloromethane using $TBAPF_6$ as the supporting electrolyte (**Figure 4**). Metallosurfactants **1** and **2** show the metal reduction $E_{1/2}^{red}$ as a reversible $1e^-$ redox wave at 1.36 $V_{Ag/AgCl}$ (0.87 $V_{Fc/Fc+}$, ΔE = 0.070, $|i_{pa}/i_{pc}|$ = 0.8) and 1.35 $V_{Ag/AgCl}$ (0.88 $V_{Fc/Fc+}$, ΔE = 0.088, $|i_{pa}/i_{pc}|$ = 0.8), whereas species **3** and **4** show this process at 0.88 $V_{Ag/AgCl}$ (0.35 $V_{Fc/Fc+}$, ΔE = 0.074, $|i_{pa}/i_{pc}|$ = 0.7) and 0.96 $V_{Ag/AgCl}$(0.48 $V_{Fc/Fc+}$, ΔE = 0.082, $|i_{pa}/i_{pc}|$ = 0.9) respectively. These potentials indicate that the nitro group brings the Ru^{2+}/Ru^{3+} couple to a more positive value.[25] The noticeable shift of *ca*. 0.50 V in species **3** and **4** is attributed to the σ donor ability of the chloride ligand, which increases the electron density around the metal center.[20d, 21a, 22, 28] The cathodic region of the CV displays multiple reduction processes ascribed to ligand-based radical anions.[20c] Species **1** shows two reduction waves at -1.19 $V_{Ag/AgCl}$ (-1.66 $V_{Fc/Fc+}$, ΔE = 0.072, $|i_{pa}/i_{pc}|$ = 1.0) and -1.50 $V_{Ag/AgCl}$ (-1.98 $V_{Fc/Fc+}$, ΔE = 0.088, $|i_{pa}/i_{pc}|$ = 1.2), corresponding to terpyridine reduction into terpyridinium radical states. Similar behavior was observed for **2,** where the two terpyridine reduction potentials are slightly shifted by approximately 0.1 and 0.04 V. However, **2** shows an additional quasi-reversible redox wave at -0.92 $V_{Ag/AgCl}$ (-1.40 $V_{Fc/Fc+}$, ΔE = 0.086, $|i_{pa}/i_{pc}|$ = 1.5) tentatively associated with the reduction of the nitro group.[19] Compounds **3** and **4** show analogous behavior to **1** and **2,** respectively. Based on previous studies, the terpyridine gets reduced at a lower potential than phenanthroline.[21a] Hence, the first process for **3** at -1.38 $V_{Ag/AgCl}$ (-1.91 $V_{Fc/Fc+}$, ΔE = 0.078, $|i_{pa}/i_{pc}|$ = 2.6) is attributed to terpy reduction, whereas the process at -1.85 $V_{Ag/AgCl}$ (-2.40 $V_{Fc/Fc+}$) is assigned to reduction of phenanthroline. Species **4** exhibits terpy/phen reductions at -1.23 $V_{Ag/AgCl}$ (-1.71 $V_{Fc/Fc+}$, ΔE = 0.082, $|i_{pa}/i_{pc}|$ = 2.6) and -1.60 $V_{Ag/AgCl}$ (-1.96 $V_{Fc/Fc+}$) respectively. Moreover, the nitro group reduction in **4** occurs at 0.58 $V_{Ag/AgCl}$ (-1.06 $V_{Fc/Fc+}$, ΔE = 0.098, $|i_{pa}/i_{pc}|$ = 1.2). The more positive nitro reduction in **2** and **4** suggests that the lowest unoccupied MO in these molecules has a predominant nitro-based component. The nitro-substituted **2** and **4** display a visible anodic shift of all potentials that may be favorable to directional electron transport.

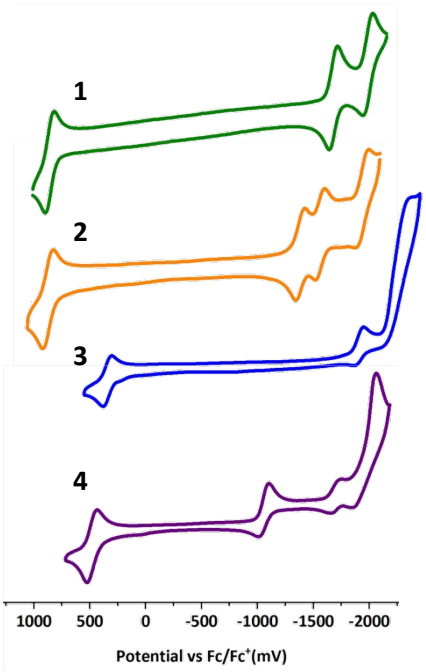

Figure 4: Cyclic voltammogram of **1-4** in 10^{-3}M dichloromethane. Glassy carbon, working electrode; Ag/AgCl, reference electrode; Pt wire, auxiliary electrode; 0.1 M $TBAPF_6$ electrolyte.

Electronic and redox DFT modeling

Theoretical calculations were performed at the B3LYP-D3/SDD,6-311G* level of theory in order to understand the ground state electronic structure and extent of metal-ligand orbital mixing associated with frontier molecular orbitals of $[Ru^{II}(C_{18}OPh\text{-}terpy)(terpy)](PF_6)_2$ **(1),** $[Ru^{II}(C_{18}OPh\text{-}terpy)(NO_2Ph\text{-}terpy)](PF_6)_2$ **(2),** $[Ru^{II}(C_{18}OPh\text{-}terpy)(phen)Cl]PF_6$ **(3)**, and $[Ru^{II}(C_{18}OPh\text{-}terpy)(NO_2\text{-}phen)Cl]PF_6$ **(4)** . The Ru^{II} center was modeled as a low spin $4d^6$ singlet (S = 0) ion with approximate electronic configuration $t_{2g}^6\ e_g^0$ in a pseudo-octahedral ligand field. The pseudo-O_h field is further idealized for species **3** and **4**. For simplicity of the calculations, the -$O(CH_2)_{17}CH_3$ group of $terpy^{OC18}$ ligand was replaced by the -OCH_3 group in the calculated model. The fragment molecular orbital (FMO) analysis was performed on complexes **1-4** to evaluate the extent of orbital mixing between metal and ligand components. Four fragments were considered for the species **1** and **2**, namely Ru, H_3C-OPh-terpy, NO_2Ph-terpy and terpy, while species **3** and **4** were divided into five fragments, namely Ru, H_3C-OPh-terpy, phen, NO_2-phen, and chloride. Relevant MOs for species **4** are shown in **Figure 5(a)-(b)**, while MOs for **1-4** are displayed in **Figures S20-21**.

In **1** and **2** the HOMO and HOMO-3 display mixed character with significant contributions from both the metal-based t_{2g} orbital and a π orbital based on the MeO-terpyridine ligand, while the HOMO-1 and HOMO-2 are predominantly a t_{2g} MO, with 68% to 72% contributions from the metal. The LUMOs of **1** and **2** are localized on the substituted terpyridine with 82% and 93% contributions, respectively. Notably, the presence of a nitrobenzene terpy has a mild effect in decreasing the LUMO energy in **2** relative to **1** by 0.3 eV, suggesting that the reduction of **2** should be somewhat facilitated. Going from **1** and **2** to species **3** and **4**, the replacement of the terpy environment by a phen/Cl^- coordination sphere leads to significant changes. It reduces the orbital interactions between the metal-based t_{2g} orbitals and the MeO-terpy-based π orbitals, yielding HOMO and HOMO-2 as predominantly (57-76%) metal-based. The HOMO and HOMO-1 display σ-donor interactions between the metal and the chlorido ligand. The presence of a nitro-substituent in **4** decreases the energy of the π* orbitals of the phenanthroline, bringing their energy below that of the equivalent terpy-based MOs. Electrochemical potentials for **1-4** were calculated in a dichloromethane implicit field, reproducing the overall experimental trends despite some discrepancy with the measured values. **Table T5** summarizes the results. A natural orbital (NO) analysis was performed on each species (**Figure S23-S26**) to aid with the assignment of the oxidation and reduction events. All metallosurfactant complexes show a reversible oxidation at positive potentials where the half-wave potentials at 1.28, 1.34, 0.50, and 0.58 $V_{Fc/Fc+}$ respectively for **1**, **2**, **3**, and **4** correspond to the metal-centered oxidation for the Ru^{II}/Ru^{III} couple. Species **1** and **3** show two reversible processes due to successive 1e^- reductions at terpy and phen, respectively, while **2** and **4** show three reduction processes due to the presence of the redox active NO_2 substituent. The first and second reduction potentials for **1** are assigned to the distinct terpy ligands, while species **3** engages both terpy and phen ligands. Thus, the most negative potentials for **2** and **4** are assigned to the nitro substituent, the second most negative process is attributed to the MeO-terpy ligands present in both species, and the least negative reduction potentials are assigned to the nitro-substituted terpy and phen ligands, respectively.

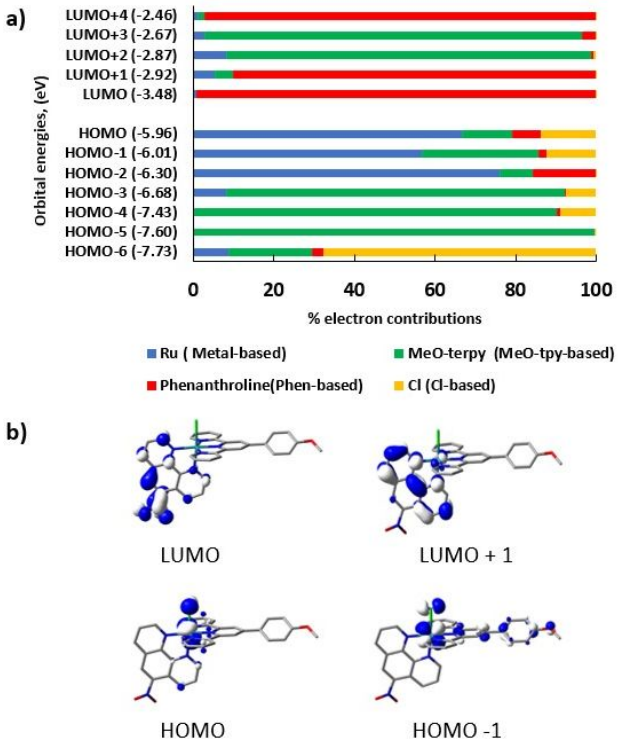

Figure 5: DFT results for the $^{LS}4d^6$ singlet (S = 0) species **4:** (a) Fragment orbital analysis; (b) Ground state frontier molecular orbitals.

Interfacial behavior and formation of Pockels-Langmuir monolayers

The amphiphilic nature of species $[Ru^{II}(C_{18}OPh\text{-}terpy)(terpy)](PF_6)_2$ **(1),** $[Ru^{II}(C_{18}OPh\text{-}terpy)(NO_2Ph\text{-}terpy)](PF_6)_2$ **(2)**, $[Ru^{II}(C_{18}OPh\text{-}terpy)(phen)Cl]PF_6$ **(3)**, and $[Ru^{II}(C_{18}OPh\text{-}terpy)(NO_2\text{-}phen)Cl]PF_6$ **(4)** and the homogeneity of the Pockels-Langmuir films[29] formed at the air|water interphase were evaluated through compression isotherms and Brewster angle microscopy (BAM) images shown in **Figures 6, S10, S11, and Table T3**. During isothermal compression, molecules of **1** show complex behavior with a possible phase rearrangement around 5-7 mN/m when the average molecular area decreases from 120 to 100 Å, followed by another phase transition around 20 mN/m with an average area of 90-92 $Å^2$, which leads to a Ries-type constant area collapse.[30] The collapse is clearly observed by BAM micrographs via the formation of ridges and Newton rings, respectively indicative of monolayer folding and the presence of generalized points of matter ejection. Species **2** starts molecular interactions at 110 Å and do not show any obvious phase transition.

The film breaks at 25 mN/m via constant pressure collapse displaying an average molecular area of 100 Å^2.

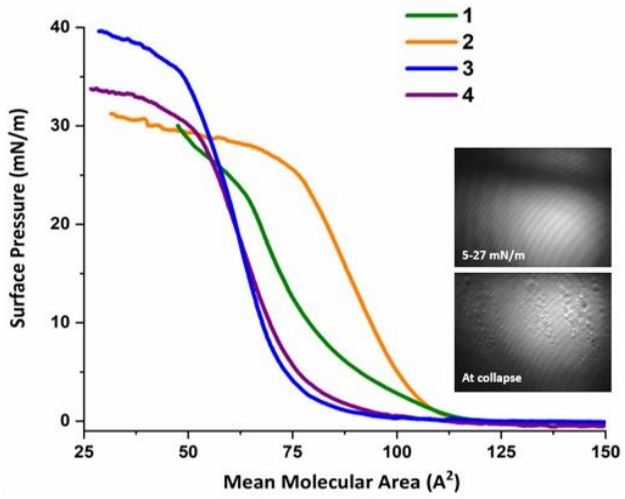

Figure 6: Compression isotherms of metallosurfactants **1-4** and BAM images of **4.**

Even at collapse the BAM micrographs reveal small points of ejection. These metallosurfactants contain two terpyridine ligands that lead to low collapse pressures and high average molecular areas around collapse pointing out to poorly organized films. Because the ligands C_{18}OPh-terpy and NO_2Ph-terpy show some water solubility, they may confer a predominantly hydrophilic character to these species leading to solubilization in the aqueous subphase. This behavior has been observed in similar Ru-terpy systems containing a bipyridine coligand by us and others.[31] Remarkably, species **3** and **4** contain the more π-saturated and hydrophobic phen ligand, and enable the formation of more ordered films. Species **3** shows no phase transitions upon isothermal compression and show clear BAM micrographs with an average molecular area of 80 Å^2, which is retained at constant pressure collapse between 30-33 mN/m. At collapse no obvious ridges are observed, but clear ejection points are observed as Newton rings. Species **4** shows similar behavior with a nominally lower collapse at 29-30 mN/m and similar average molecular areas between 77 and 80 Å^2. These results suggest the formation of more ordered monolayers at the air|water interface. Understanding the behavior of these Pockels-Langmuir films allowed for their transfer onto air|solid substrates and investigation of the equivalent Langmuir-Blodgett monolayers required for junction fabrication.

Morphological analysis of the deposited Langmuir-Blodgett films

To identify the most appropriate deposition pressure of the LB film aiming at junction fabrication, monolayers of surfactants [Ru^{II}(C_{18}OPh-terpy)(phen)Cl]PF_6 **(3)**, and [Ru^{II}(C_{18}OPh-terpy)(NO_2-phen)Cl]PF_6 **(4)** were deposited on mica substrates and analyzed by atomic force microscopy (AFM). We started with species **4**, where LB films were deposited at surface pressures of 17, 20, 24, and 28 mN/m. **Figure 7** shows the associated AFM images, where films deposited at the lowest and highest pressures show rougher surfaces ~0.30 nm indicating respectively the presence of pin hole defects or formation of multilayer spots. On the other hand, films deposited at 20 mN/m display a smooth surface with roughness ~0.12 ± 0.1 nm representative of a homogeneous topology and considered appropriate for use in junctions. Interestingly, species **3** delivered obvious pinholes at 18 and 23 m/Nm with the most suitable monolayer being achieved at the higher pressure of 27 mN/m. It is noteworthy that the best LB film for species **3** still shows roughness 0.26 ± 0.5 nm.

The structural properties of deposited films were further analyzed through infrared reflection absorption spectroscopy (IRRAS), UV-visible spectroscopy (UV-visible), and electrospray ionization mass spectroscopy (ESI-MS) methods. Multilayer films were used for these analyses owing to limitations imposed by the detection threshold of the instruments on monolayers. The films were deposited *via* the Y-type dipping method, where the interactions between adjacent monolayers are hydrophilic-hydrophilic or hydrophobic-hydrophobic in nature. During the deposition process, species **1** and **2** exhibited transfer ratios smaller than the unity indicating incomplete film transfer onto solid substrates.[32] Together with lower collapse pressures, these inadequate surface properties render these species ill-suited for junction fabrication because the uncovered portions of the gold substrate will lead to short circuits, and were not pursued further. Metallosurfactants **3** and **4** were further analyzed, and **Figure 8** and **Figures S14-S15** show the comparative spectra for infrared (FT-IR) of the bulk species and the IRRAS of the deposited multilayers taken at an angle of incidence of 40° under s-polarized light. The peak pattern observed for the film is similar to that of the bulk material, although the increased order observed in the film leads to minor shifts and splittings of some vibration modes. Overall, the data confirms the absence of significant structural changes for the metallosurfactants during film deposition. Characteristic peaks corresponding to symmetric and asymmetric stretching vibrations of CH_2 groups were observed at 2920 cm^{-1} and 2850 cm^{-1}. The fingerprint region of both bulk and film samples displays aromatic C=C, C-H vibration peaks at 1602 cm^{-1}, 1595 cm^{-1}, and 1532 cm^{-1}.

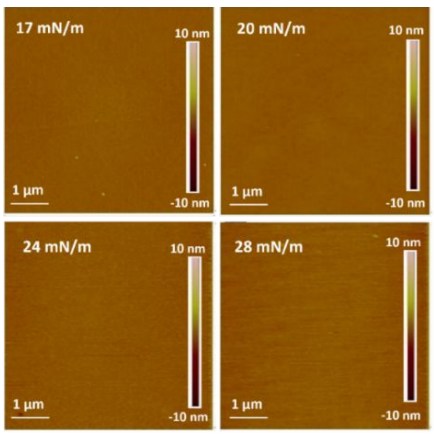

Figure 7: AFM images of **4** at 17, 20,24 and 28 mN/m.

The stretching vibration detected at 1537 cm^{-1} for LB film of **4** confirms the presence of nitro (-NO_2) substituents in the ligand environment. Moreover, the counter ion PF_6^- peak observed at 847 cm^{-1} in the IRRAS of both **3** and **4** validates that these metallosurfactants remain neutral species after the deposition. The peak pattern of the thin films displays the presence of positive and negative bands in agreement with IRRAS surface selection rules.[33] A positive peak in upward position is observed for a transitional dipole moment of a functional group with a surface-perpendicular component with respect to the dielectric substrate, whereas the surface-parallel component of a transition moment yields a negative downward band. Consequently, this allows us to infer the orientation of the thin film on the solid sample. The CH_2 stretching vibration peaks of both complexes show a negative band, indicating that both symmetric and asymmetric modes of this vibration have dipole moments parallel to the surface. Considering the compact nature of these molecules, it can be deduced that alkyl chains have a perpendicular orientation to the surface. The opposite was observed for the nitro group vibrational peak, indicating that the N-O vibration has a dipole momentum parallel to the surface.

The UV-visible spectroscopic data of the thin films containing 47 layers of **3** and **4** is shown in **Figures S12** and **S13**. The films retain similar processes discussed in the previous section, albeit revealing minor red-shifting and broadening of peaks consistent of J-type aggregate formation during the multilayer deposition.[34]

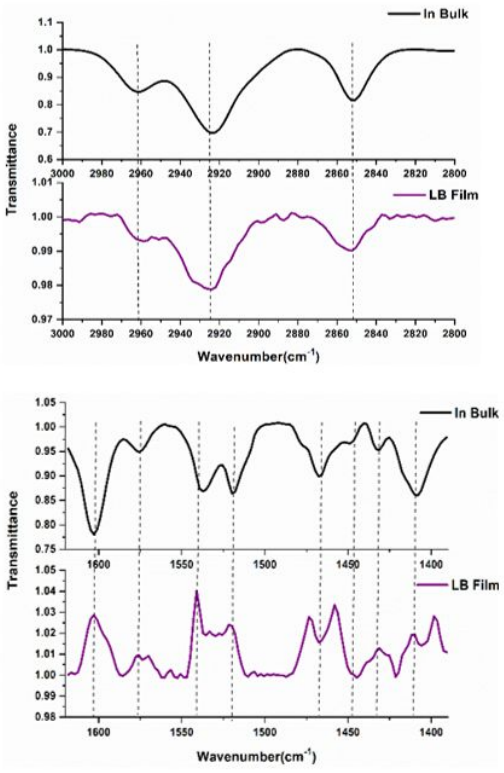

Figure 8: Comparison between IR spectrum of metallosurfactant **4** in KBr and IRRAS spectrum of 47-layer LB film

Further characterization of the LB films was performed in order to establish the molecular stability of the deposited metallosurfactants. The films were mechanically scraped off, dissolved in acetonitrile and analyzed by ESI-MS spectrometry. The results shown in **Figures S16** and **S17**, confirm the presence of the expected molecular ion peaks for both **3** and **4**, along with the characteristic isotopic distribution envelope.

Assessment of orbital availability for electron transport

The availability of frontier orbitals with appropriate energies near the estimated Fermi levels of the gold electrodes is a necessary condition for electron transfer. An applied negative bias increases the Fermi energy of the Au electrode (*i.e.* gets closer to zero), also lifting the energies of the neighboring MOs. The energy of the biased electrode cannot be calculated with precision, but the relative MO energies can be estimated from the experimental redox potentials given in V and converted to solid-state potentials in eV, according to models proposed by Tour, Hipps, and Armstrong.[11-12, 35]

$$V_i = 4.7\ eV + (1.7)\ E_{1/2}{}^{ox}{}_{SCE} \quad (Eq.1)$$

$$V_a = 4.7\ eV + E_{1/2}{}^{red}{}_{SCE} \quad (Eq.2)$$

Here, the HOMO and LUMO energy levels of each metallosurfactant were calculated based on the available cyclic voltammetric data. The $E_{1/2}{}^{ox}{}_{SCE}$ and $E_{1/2}{}^{red}{}_{SCE}$ represent the first oxidation and reduction half-wave potentials of the metallosurfactants *vs.* saturated calomel electrode potentials (SCE), while the values of V_i and V_a closely represent the first ionization and first electron affinity energies of the molecular species, respectively. The V_i and V_a energies are analogous to respective first metal-centered HOMO and first ligand-centered LUMO levels. The calculated MO energies for [Ru^{II}(C_{18}OPh-terpy)(terpy)]$(PF_6)_2$ **(1),** [Ru^{II}(C_{18}OPh-terpy)(NO_2Ph-terpy)]$(PF_6)_2$ **(2),** [Ru^{II}(C_{18}OPh-terpy)(phen)Cl]PF_6 **(3)**, and [Ru^{II}(C_{18}OPh-terpy)(NO_2-phen)Cl]PF_6 **(4)** are summarized in **Figure 9**. According to this diagram, the HOMO levels of metallosurfactants **1** and **2** were calculated respectively as -7.0 and -6.9 eV, and the LUMO levels respectively at -3.5 and -3.7 V. Considering the Fermi level of the Au electrode to be -5.1 eV below vacuum, the HOMO level of both species is about 2 eV below the Fermi level, whereas the LUMO level of **1** and **2** lies 1.6 and 1.4 eV above the Fermi level, respectively. This behavior is consistent with previous studies on similar bis-terpy ruthenium systems, suggesting that the HOMO level of these species is predominantly based on the ruthenium t_{2g} orbitals with a small contribution from the terpy ligand. This is in good agreement with the DFT calculations discussed previously and explains the observation of comparable HOMO energies between **1** and **2**, in spite of the presence of a nitro substituent in **2**. The presence of a benzyl ring spacer between terpy and -NO_2 renders the electron-withdrawing behavior of the nitro group negligible. For species **1**, the LUMO orbital is mostly localized on the terpy and is antibonding (π^*) in nature, while species **2** has a LUMO level that is

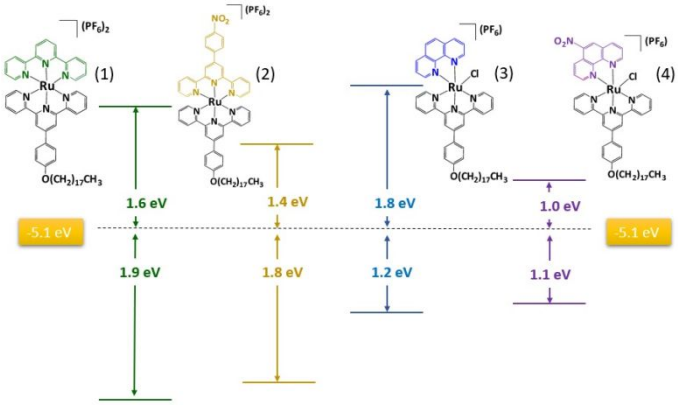

Figure 9: Frontier molecular orbital energy diagram for metallosurfactants **1-4.**

slightly lower than the terpy-based π* MO and is based on π* orbitals of the nitrophenyl ring. Therefore, regardless of having a strong electron-withdrawing nitro substituent, this is electronically isolated and does not affect significantly the LUMO energy level, as originally thought possible.

The HOMOs of **3** and **4** are considerably higher than those in **1** and **2** by a 0.7 eV difference. This is ascribed to the π-donor ability of the Cl^- group, which shows an antibonding interaction with the ruthenium-based t_{2g} MO. Moreover, the HOMOs in these species are nearly isoenergetic at 1.1 and 1.2 eV confirming that the nitro group does not have a significant effect on the oxidation events. On the other hand, the LUMO energies in compounds **3** and **4** show a sizable difference of 0.8 eV from each other. As for **1** and **2**, the LUMO of **3** is mainly terpy-based, whereas for **4** it is localized along the nitro group. As such, the effect of the nitro group is much more pronounced in **4** than in **2**, due to the absence of an isolating benzene group and to the higher degree of conjugation in the planar phenanthroline ligand.

Electron transport in Au|LB|Au junctions

Understanding the most appropriate deposition pressures allowed for the assembly of nanoscale electrode|LB film|electrode junctions containing metallosurfactants $[Ru^{II}(C_{18}OPh\text{-}terpy)(phen)Cl]PF_6$ **(3)**, and $[Ru^{II}(C_{18}OPh\text{-}terpy)(NO_2\text{-}phen)Cl]PF_6$ **(4)**, and for assessing the current-voltage (I/V) characteristics associated with charge transport. A single LB monolayer of the surfactant was deposited onto a gold-coated mica substrate; a surface pressure of 27 mNm^{-1} was used for **3** and 20 mNm^{-1} for **4** and the junctions were completed by the deposition of a top gold electrode using shadow masking sputtering.[16a, 36] Three assemblies with 16 individual Au|LB**3**|Au and Au|LB**4**|Au junctions were prepared for each metallosurfactant totalling 48 junctions each. During the I/V measurement, bias voltage was applied to the top Au electrode while retaining the voltage of the bottom Au electrode at zero. Characteristic responses are shown in **Figures 10** and **S27**. The Au|LB**3**|Au junction yielded a response akin to an insulator-like behavior with negligible current response. The LUMO energy was calculated at 1.8 eV and our group has previously reported a similar negligible current response observed for the square-planar $[Cu^{II}(L^{N2O2})]$ species with a comparable LUMO-Fermi energy gap of 1.9 eV.[36] We proposed that the copper(II) species with a $3d^9$ configuration cannot involve fully occupied HOMOs, but rather rely on electron transport trough the only available singly-occupied MO, namely the metal-based $3d_{x2-y2}$. Accordingly, although the HOMO level of **3** is 1.2 eV, and therefore closer to the Fermi level than the LUMO level, the absence of a prominent current response in the positive quadrant of the I/V curve indicates that the HOMO orbital does not engage in electron transport. This is in excellent agreement with the work of Lacroix *et al*.[37] on ruthenium polypyridine complexes, $[Ru(bpy)_2ppy]^+$ and $[Ru(bpy)_3]^{2+}$, which suggests that the HOMO does not have a significant effect on the electron transport process of thin films. On the other hand, species **4** has a calculated Fermi/HOMO gap of 1.1 eV and Fermi/LUMO gap of 1.0 eV, thus within the usual region in which we observe directional electron transport. Indeed, about 40%, or 18 out of 48 Au|LB**4**|Au junctions showed an asymmetric I/V behavior with higher current in the negative quadrant of the curve as opposed to negligible current in the positive quadrant. The rectification ratio given by RR=[I at -V/ I at +V] for these Au|LB**4**|Au junctions varies from 5 to 26 between -1 to +1 V and from 3 to 14 between -3 to +3 V, respectively, while the maximum current varies from negligible (-0.04 nA at ±1 V in assembly 2) to substantial (-2.0 nA at ±4 V in assemblies #1, #2, and #3). The directionality of the transport was further confirmed by reversing the source and drain electrodes; this inversion led to a similarly directional but reversed I/V response. Upon increasing the applied bias voltage, the rectification ratio of metallosurfactant **4** decreases, demonstrating a sigmoidal I/V response. This behavior is tentatively attributed to random reorientation of the molecules in the film at higher potentials to stabilize the overall energy of the monolayer.

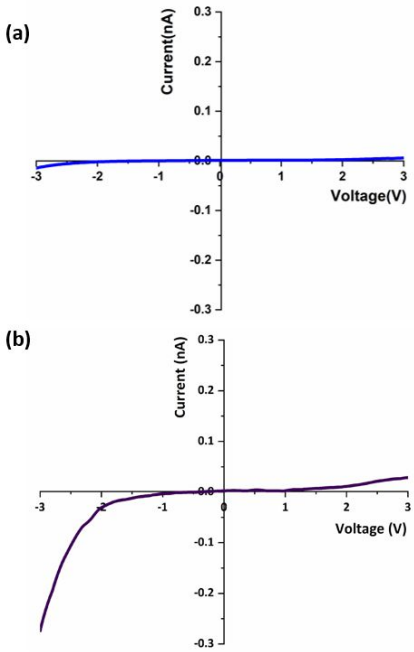

Figure 10: I/V curves for (a) **3**, (b) **4** at ± 3 V.

The energies of the frontier orbitals in **3** and **4** have been calculated by DFT methods to aid in understanding the pathways of directional electron transfer and are shown in **Figures S22-26**. The HOMO is metal-based in both metallosurfactants, and therefore assigned to a low-spin $(t_{2g})^6$-like MO set. Interestingly, in both cases the metal LUMO assigned to the e_g-like MO set is much higher in energy than the ligand-based orbitals and cannot participate in electron transport. The closest LUMOs to the estimated resting Fermi levels of the gold electrode vary in each of these species. In the unsubstituted **3** it is delocalized over the terpy ligand, whereas the phen-based unoccupied MO is higher in energy and therefore unattainable. However, the presence of an electron-withdrawing nitro substituent in **4** lowers significantly the energy of the phen-based orbitals. We propose that electron transport takes place *via* the phen-based LUMO orbital whose energy is modulated by the NO_2 substituent, and now comparable to the Fermi levels of the electrode. This situation is similar to that of our recently reported $[Ru^{III}(L^{terpy})(SQ)Cl]PF_6$ system[17], in which a low lying LUMO primarily associated with the semiquinone ligand SQ, can partake in directional electron transport. This behavior is distinctive from the temperature-dependent Kondo effect observed for electron transport in the $[Co^{II}(S\text{-terpy})_2]$ species studied by Park *et al.*[3] and from the configuration-dependent electron transport described by van der Zant *et al*.[5] for a $[Mn^{II}(S\text{-terpy})_2]$. However, those species contain first-row metals centers with respective $^{HS}3d^7$ cobalt(II) and $^{HS}3d^5$ manganese(II) configurations and smaller ligand fields. The behavior of those species is well in tune with our non-terpy based phenolate-rich $^{HS}3d^5$ iron(III) metallosurfactants,[35] in which transport takes place through the metal-based singly occupied SOMO. The behavior of species **4** bears similarity with the recently described $3d^3$ chromium(III) species[38] in which ligand oxidation leads to the formation of a phenoxyl-based SOMO capable of transport. Although the magnitude of the currents in **4** and in $[Ru^{III}(C_{18}\text{-Ph-terpy})(SQ)Cl]PF_6$ are different, the asymmetric current response is comparable to that for a donor/acceptor dyad reported by Lacroix *et al.*[15] encompassing a (terpy)Ru/naphthalenediimide species. Although the exact mechanism of transport was beyond the scope of that study, our results suggest that that the pathways could involve exclusively the LUMO of the naphthalenediimide.

Conclusion

The heteroleptic metallosurfactants $[Ru^{II}(C_{18}OPh\text{-terpy})(terpy)](PF_6)_2$ **(1),** $[Ru^{II}(C_{18}OPh\text{-terpy})(NO_2Ph\text{-terpy})](PF_6)_2$ **(2)**, $[Ru^{II}(C_{18}OPh\text{-terpy})(phen)Cl]PF_6$ **(3)**, and $[Ru^{II}(C_{18}OPh\text{-terpy})(NO_2\text{-phen})Cl]PF_6$ **(4)** were obtained by stepwise synthesis and characterized to study the effect of electron-withdrawing nitro substituents in modulating the energy of the frontier orbitals to approach or match the Fermi levels of the gold electrode for directional electron transport. The combined electronic, redox, and DFT data supports that the frontier molecular orbital energies associated with these species can be successfully modulated. The MO diagram for **2** and **4** suggest extensive electron delocalization over the $-NO_2$ containing terpy or phen ligand, which contributes to more than 80% of the LUMO orbital. Although species **1** and **2** yield unsuitable films that prevent the development of junctions for further analysis, a comparison of electron transport behavior was carried out in Au|LB**3**|Au and Au|LB**4**|Au junctions. Distinctly contrasting electron transfer properties of **3** and **4** suggest that the matching energies between the LUMO and Fermi levels is imperative in attaining directional electron transfer through molecules. As such, **3** shows negligible electron transport with its terpy-based LUMO mismatching the Fermi levels by 1.8 eV, while species **4** shows directional electron transport through the NO_2phen-based LUMO that becomes available within 1.0 eV from the resting Fermi level. The results validate our hypothesis that the installation of electron-withdrawing substituents may lead to lowering of unoccupied MOs and enable directional electron transport in 4d-based metallosurfactants and offer an alternative pathway for electron transport in 4d metallosurfactants that take advantage of low-lying unoccupied MOs.

Experimental Section

Materials and Methods

Solvents and chemical reagents were used as obtained from commercial sources. 2-acetylpyridine, 4-octadecyloxy benzaldehyde, and 5-nitrophenanthroline were purchased from TCI Chemicals, 1,10-phenanthroline was purchased from Alfa Aesar, 2,2':6'2"-terpyridine was purchased from GFS Chemicals, $RuCl_3.6H_2O$ was purchased from Oakwood Chemical. ^{1}H-NMR, ^{13}C-NMR, COSY-NMR, and HSQC-NMR data were collected in CD_2Cl_2 using a Varian 600 MHz spectrometer. Electrospray ionization mass spectroscopy (ESI-MS) data were collected using a Waters-ZQ 2695. Infrared (IR) and IR-reflection/absorption (IRRAS) spectra were respectively measured as KBr pellets and thin films using a Tensor 27 FTIR spectrometer at a wavelength range of 4000 to 400 cm^{-1}. Elemental analyses were measured by Midwest Microlab, Indianapolis, IN. Cyclic voltammetry experiments were performed using either a BAS 50W or a CH Instruments potentiostat with a standard three-electrode cell consisting of a platinum wire auxiliary electrode, Glassy carbon working electrode, and Ag/AgCl in saturated KCl as reference electrode. Experiments were conducted under argon at room temperature using $TBAPF_6$ as the supporting electrolyte. All the potentials were referenced according to the potential of the internal standard ferrocene.[39] The electronic spectra were recorded in 10^{-4} M dichloromethane solutions using a UV-3600 Shimadzu spectrophotometer in the range of 190-1600 nm.

Syntheses.

4'-(4-octadecyloxyphenyl)-2,2':6',2"-terpyridine (terpy^{OC18}). The ligand was synthesized according to the Kröhnke method.[40] Two equivalents of 2-acetyl pyridine (0.61 g: 4.90 mmol) were treated with one equivalent of 4-octadecyloxy benzaldehyde (0.93 g: 2.50 mmol) in ethanol (25 mL), and in presence of two equivalents of KOH (0.30 g: 5.40 mmol) and NH_4OH (7.4 mL). The reaction mixture was refluxed for 4 h at 60 °C. The off-white precipitate was washed with water and recrystallized in absolute ethanol to yield a white product.

Yield = 30 %. ZQ-MS (m/z$^+$) = 576.93 (100%) for [$C_{39}H_{51}N_3O$] (calculated = 577.86). FTIR (KBr cm^{-1}) 2850-2920 (ν_{C-H}), 1584-1516 ($\nu_{C=C}$, aromatic), 1469 ($\nu_{C=N}$, aromatic). ^{1}H NMR, ppm (CD_2Cl_2, 400 MHz) δ 8.74 (m,6H), δ 7.89 (m,4H), δ 7.38 (t,2H), δ 7.05 (d,2H), δ 4.06 (t,2H), δ 1.83 (t,2H), δ 1.28 (m,30H), δ 0.89 (t,3H).

4'-(4-nitrophenyl)- 2,2':6',2"-terpyridine (terpy^{NO2}). Preparation of this ligand involves three steps; the precursors (E)-3-(4"-nitrophenyl)-1-(pyrid-2'yl)prop-2-enone and pyridacyl pyridinium iodide are synthesized followed by cyclization to obtain the final ligand.[18a]

i. Synthesis of (E)-3-(4"-nitrophenyl)-1-(pyrid-2'yl)prop-2-enone. 4-nitrobenzaldehyde (2.40 g: 15.80 mmol) was added to a solution of 2-acetyl pyridine (1.85 g: 15.30 mmol) in ethanol (20 mL). Then sodium hydroxide (0.5 mL, 10% aq) was added and the reaction mixture stirred for 4 h at 0 °C. The off-white precipitate was washed with cold ethanol and recrystallized in boiling ethanol to yield yellow needle-like crystals. Yield = 21%. FTIR (KBr cm^{-1}) 1671 (($\nu_{C=O}$), 1609 ($\nu_{C=C,}$ aromatic), 1511, 1341 (ν_{N-O}). ^{1}H NMR, ppm ($CDCl_3$, 400 MHz) δ 8.76 (d, 1H), δ 8.41 (d, 1H), 8.26 (d, 2H), 8.20 (d, 1H), 7.88 (m, 4H), 7.55 (m, 1H).

ii. Synthesis of pyridacyl pyridinium iodide. 2-acetyl pyridine (6.40 g: 0.50 mol) was added to a solution of I_2 (12.70 g: 0.50 mol) in dry pyridine (60 mL). This reaction mixture was refluxed for 1 h and then cooled in an ice bath to obtain a black precipitate. This product was filtered and washed with an ether:ethanol (9:1) solvent mixture and subsequently redissolved in hot methanol. It was refluxed for 1 h in the presence of activated carbon. The resulting solution was filtered through celite while hot and kept in the refrigerator to obtain yellow needle-like crystals. The product was washed with cold methanol and dried under vacuum. Yield = 10%. FTIR (KBr cm^{-1}) 3052, 2877 ($\nu_{C=H}$), 1710 ($\nu_{C=O}$), 1631 ($\nu_{C=N}$), 1482($\nu_{C=C,}$ aromatic). ^{1}H NMR, ppm (DMSO, 400 MHz) δ 8.98 (d, 2H), δ 8.86 (d, 1H), 8.71 (t, 1H), 8.26 (t, 2H), 8.12 (t, 1H), 8.07 (d, 1H), 7.82 (m, 1H), 6.49 (s, 2H).

iii. For the synthesis of the ligand, (E)-3-(4"-nitrophenyl)-1-(pyrid-2'yl)prop-2-enone (0.25 g: 1.00 mmol) and Pyridacyl pyridinium iodide (0.32 g: 1.00 mmol) were dissolved in methanol (20 mL) at 60 °C. Ammonium acetate (0.40 g: 7.80 mmol) was added and the reaction mixture was refluxed for 12 h. The crude product was recrystallized in ethanol to obtain a pure off-white color product. Yield = 55%. ZQ-MS(m/z$^+$) = 355 (100%) for [$C_{21}H_{14}N_4O_2$] (calculated= 354.37). FTIR (KBr,cm^{-1}) 1585, 1469, 1416 ($\nu_{C=N, C=C}$), 1513, 1352 (ν_{N-O}). ^{1}H NMR, ppm ($CDCl_3$, 500 MHz) δ 8.76 (s ,2H), δ 8.74 (d ,2H), δ 8.70 (d ,2H), δ 8.37 (d ,2H), δ 8.05 (d ,2H), δ 7.91 (dt ,2H), δ 7.40 (dd ,2H). Melting point = 210 °C.

Synthesis of the metallosurfactants 1-4

$Ru(DMSO)_4Cl_2$. $RuCl_3.6H_2O$ (2.00 g: 9.64 mmol) was dissolved in DMSO (25 mL) under argon at 80 °C. The solution was refluxed until the deep red color of the solution changed to orange. After cooling down to room temperature, acetone (40 mL) was added dropwise to the reaction mixture. The final mixture was cooled in an ice bath to obtain a yellow precipitate. Yield = 43%

Ru(C_{18}OPh-terpy)(DMSO)Cl_2. One equivalent of $Ru(DMSO)_4Cl_2$ (0.22 g: 0.46 mmol) was treated with one equivalent of 4'-(4-octadecyloxyphenyl)-2,2':6',2"-terpyridine (0.25 g: 0.43 mmol) in 20 mL ethanol under dark conditions. The solution was refluxed for 18 h under argon. The crude product was obtained as a dark brown solid that was washed with cold ethanol and water and dried under vacuum. Yield = 53%. FTIR (KBr, cm^{-1}) 2922, 2852 (long chain C-H), 1603, 1519, 1467, 1402 (pyridine rings), 1080 (S=O). ^{1}H NMR, ppm (CD_2Cl_2, 400 MHz) δ 9.27 (d, 2H), δ 8.19 (d, 4H), δ 7.96 (t, 2H), δ 7.78 (d, 2H), δ 7.63 (t, 2H), δ 7.06 (d, 2H), δ 4.06 (t, 2H), δ 2.75 (s, 6H), δ 1.85 (t, 2H), δ 1.28 (m, 30H), δ 0.89 (t, 3H).

[Ru^{II}(C_{18}OPh-terpy)(terpy)]$(PF_6)_2$ (1). Ru(C_{18}OPh-terpy)(DMSO)Cl_2 (0.40 g: 0.48 mmol) was dissolved in Ar-degassed ethanol. 2,2';6',2"-terpyridine (0.11 g: 0.42 mmol) was added to this solution and the reaction mixture was refluxed for 18 h under dark conditions. After addition of NH_4PF_6 (0.18 g: 1.10 mmol), the product was precipitated as a dark red solid and further purified on a chromatography column using neutral alumina with dichloromethane:acetonitrile (4:1). Yield = 51%. ZQ-MS(m/z$^+$) = 455.95 (100%) for [$C_{55}H_{65}RuN_6O]^{2+}$ (calculated= 456). FTIR (KBr, cm^{-1}) 2923, 2852 (long chain C-H), 1604, 1519, 1436, 1388 (Pyridine rings), 840 (PF_6^-). ^{1}H NMR, ppm (CD_2Cl_2, 600 MHz) δ 8.81 (s, 2H), δ 8.69 (s, 2H), δ 8.51 (d, 2H), δ 8.44 (d, 2H), δ 8.10 (d, 2H), δ 7.92 (q, 4H), δ 7.40 (d, 2H), δ 7.30 (d, 2H), 7.24 (m, 6H), δ 4.15 (t, 2H), δ 1.88 (m, 2H), δ 1.29 (s, 30H), δ 0.90 (t, 3H).

[Ru^{II}(C_{18}OPh-terpy)(NO_2Ph-terpy)]$(PF_6)_2$ (2). Ru(C_{18}OPh-terpy)(DMSO)Cl_2 (0.34 g: 0.42 mmol) was dissolved in Ar-degassed ethanol. 4'-(4-nitrophenyl)- 2,2':6',2"-terpyridine (NO_2Ph-terpy) (0.15 g: 0.43 mmol) was added to this solution and the reaction mixture was refluxed for 18 h under dark conditions. After addition of NH_4PF_6 (0.16 g: 0.96 mmol), product was precipitated as a dark red color solid. Further purification was done by column chromatography using neutral alumina with 1:1 dichloromethane:acetonitrile. Yield = 41%. ZQ-MS(m/z$^+$) = 516.58 (100%) for [$C_{60}H_{65}RuN_7O_3]^{2+}$ (calculated= 516.5). FTIR (KBr, cm^{-1}) 2923, 2852 (long chain (C-H), 1604, 1519, 1436, 1388 (pyridine rings), 840 (PF_6^-).^{1}H NMR, ppm (CD_2Cl_2, 600 MHz) δ 9.06 (s, 2H), δ 8.99 (s, 2H), δ 8.66 (t, 4H), δ 8.60 (d, 2H), δ 8.42 (d, 2H), δ 8.18 (d, 2H), δ 7.98 (q, 4H), δ 7.47 (d, 2H), δ 7.41 (d, 2H), δ 7.30 (d, 2H), δ 7.22 (t, 2H), δ 7.18 (t, 2H), δ 4.19 (t, 2H), δ 1.90 (m, 2H), δ 1.29 (s, 30H), δ 0.89 (t, 3H).

[Ru^{II}(C_{18}OPh-terpy)(phen)Cl]PF_6 (3). Ru(C_{18}OPh-terpy)(DMSO)Cl_2 (0.20 g: 0.24 mmol) was dissolved in Ar-degassed ethanol. Phenanthroline (0.05 g: 0.23 mmol) was added to this solution and the reaction mixture was refluxed for 18 h under dark conditions. After addition of NH_4PF_6 (0.05 g: 0.30 mmol), product was precipitated as a dark red solid. Further purification was done by column chromatography using neutral alumina with 6:1 dichloromethane: acetone. Yield = 40 %. Elemental analysis calculated % for [$C_{51}H_{59}ClF_6N_5OPRu.H_2O$]: C 57.92, H 5.81, N 6.62;

Found: C 57.60, H 5.56, N 6.73 ZQ-MS(m/z$^+$) = 894.26 (100%) for $[C_{51}H_{59}RuN_5OCl]^+$ (calculated = 894.59). FTIR (KBr, cm^{-1}) 2923, 2852 (long chain C-H), 1602, 1519, 1466, 1427, 1407, 1388 (Pyridine rings), 846 (PF_6^-). ^{1}H NMR, ppm (CD_2Cl_2, 400 MHz) δ 10.58 (d, 1H), δ 8.72 (d, 1H), δ 8.55 (s, 2H), δ 8.30 (m, 4H), δ 8.17 (d, 1H), δ 8.07 (d, 1H), δ 7.97 (d, 2H), δ 7.82 (t, 2H), δ 7.70 (d, 1H), δ 7.52 (d, 2H), δ 7.36 (t, 1H), δ 7.18 (d, 2H), δ 7.13 (t, 2H), δ 4.13 (t, 2H), δ 1.88 (m, 2H), δ 1.29 (s, 30H), δ 0.89 (t, 3H).

[Ru^{II}(C_{18}OPh-terpy)(NO_2-phen)Cl]PF_6 (4). Ru(C_{18}OPh-terpy)(DMSO)Cl_2 (0.24 g: 0.30 mmol) was dissolved in Ar-degassed ethanol. 5-nitro phenanthroline (NO_2-phen) (0.07 g: 0.30 mmol) was added to this solution and the reaction mixture was refluxed for 18 h under dark conditions. After addition of NH_4PF_6 (0.06 g: 0.40 mmol), product was precipitated as a dark purple solid. Further purification proceeded with column chromatography using neutral alumina with 4:1 dichloromethane : acetonitrile. Yield (43%). Elemental analysis calculated % for $[C_{51}H_{58}ClF_6N_6O_3PRu.2H_2O]$: C 54.66, H 5.58, N 7.50; Found: C 54.26, H 5.32, N 7.93. ZQ-MS(m/z$^+$) = 894.26 (100%) for $[C_{51}H_{58}RuN_6OCl]^+$ (calculated= 894.59). FTIR (KBr, cm^{-1}) 2923, 2853 (long chain C-H), 1602, 1537, 1520, 1468, 1408, 1338, 1262, 1186 (Pyridine rings), 843 (PF_6^-). ^{1}H NMR, ppm (CD_2Cl_2, 600 MHz) δ 10.78 (d, 1H), δ 9.38 (d, 1H), δ 8.94 (s, 1H), δ 8.56 (s, 2H), δ 8.43 (q, 1H), δ 8.33 (t, 3H), δ 7.97 (d, 2H), δ 7,92 (d, 1H), δ 7.78 (t, 2H), δ 7.48 (t, 3H), δ 7.13 (t, 4H), δ 4.11 (t, 2H), δ 1.88 (m, 2H), δ 1.29 (s, 30H), δ 0.89 (t, 3H).

Other methods

Surfactant analysis. Development of Pockels-Langmuir and Langmuir-Blodgett monolayer films. An automated KSV Minitrough (Biolin, Espoo, Finland) was used to obtain the pressure *vs.* area (Π-A) isotherms the air/water interphase for these four metallosurfactant complexes. All experiments were performed at 23 ± 0.3°C using ultra-pure 18 MΩ.cm water from a Barnstead Nanopure system as the subphase. The Langmuir-Blodgett trough and barriers were cleaned by alternatively washing with ethanol and deionized water for three times and finally rinsing with ultra-pure water. Before the experiment, the impurities present at the surface of the aqueous subphase were removed by vacuum. The metallosurfactants were dissolved in highly volatile (dichloromethane) to prepare spreading solutions with a concentration of 1 mg/mL. Approximately 30-40 µL of spreading solution was introduced over the subphase for each trial and 20 min waiting time was maintained before monolayer compression. The barriers were compressed at a rate of 10 mm min^{-1} during each measurement and a paper Wilhelmy plate (20 x 10 mm) was used to measure the surface pressure of the isotherm. At least three reproducible measurements were recorded for each species.

Brewster angle microscopy (BAM). The BAM micrographs of these three metallosurfactants were recorded using a CCD detector in KSV-Optrel BAM 300 with a HeNe laser(10 mW, 632.8 nm). The monolayer compression rate was maintained constant throughout compression at 10 mm/min.

AFM measurements. Atomic force microscope images of the sample surfaces were taken using a Bruker Bioscope Catalyst AFM. A MicroMasch CSC 38 cantilever with a spring constant of 0.09 N m−1 was used to image the surface in contact mode imaging in air. The cantilevers were cleaned with ethanol, followed by DI water before doing an experiment. The cleaned cantilever was then mounted on a cantilever holder, and the sum signal was maximized using the easy align system. The AFM head was then placed on top of the AFM base plate where the prepared sample was placed. The cantilever was manually lowered carefully to approach the surface of the sample before engaging it automatically. The system was in rest for 5 minutes before the scan was started. Scanning used a rate of 1 Hz (10 µm s^{-1} tip velocity). Results are shown in **Figure 7**, **Figure S18** and **Table T4.**

Measurement of *I–V* curves. Nanoscale junctions were assembled using gold-coated mica substrates covered with a single Langmuir-Blodgett monolayer of metallosurfactant **3** or **4** onto gold-coated mica substrates at respective surface pressures of 27 and 20 mNm^{-1}. The Au|LB junctions and were dried for 4 days in a desiccator. The top Au-electrode was coated on an EffaCoater gold sputter using the shadow masking method.[16a] Three assemblies with 16 individual junctions were prepared for each metallosurfactant. Their electron transfer properties were measured as current *vs.* voltage (I/V) curves using a Keithley 4200 semiconductor parameter analyzer coupled to a Signatone S-1160 Probe Station. See **Figure S27**.

Computational Methods

The Ru complexes **1**-**4** were optimized using the B3LYP functional[41] with Grimme's D3 dispersion correction.[42] For simplicity of the calculations, the -O$(CH_2)_{17}CH_3$ group of terpy^{OC18} ligand was replaced by the -OCH_3 group in the calculated model (See **Figures S19-26**, and **Table T5**). The SDD effective core potential (ECP) and an associated basis set for Ru atom were used,[43] while the 6-311G* basis set was employed for all other atoms (Cl, O, N, C, and H).[44] Solvent effects (dichloromethane) were included in the calculations through polarizable continuum model (PCM).[45] The ultrafine grid was used in all calculations. Vibrational frequency analysis was performed on optimized structures to confirm their convergence to the local minima at their respective potential energy surfaces. Natural orbital (NO) analysis[46] was applied to determine the character of open-shell electronic states. The AOMix program[47] was used to perform fragment molecular orbital (FMO) analysis of asymmetric complexes in their singlet ground states. Half-wave potentials ($E_{1/2}$) were determined relative to the ferrocene/ferrocenium (Fc/Fc^+) redox couple through equation 3:

$$E°\,(eV) = -\frac{\Delta Gsol}{nF} - 5.00 \quad \text{(Eq.3)}$$

where ΔG_{sol} is the change in solvated free energy upon reduction, *n* is the number of electrons (in this case, 1), and *F* is the Faraday constant. Reduced and oxidized species were fully optimized at the same level of theory as the Ru(II) species. Multiple spin states were considered for each oxidized or reduced complex (i.e., singlet, triplet

or doublet, quartet) in order to determine the electronic state with the lowest energy. The calculated redox potentials are referenced to the Fc/Fc^+ by subtracting the estimated absolute reduction potential of Fc/Fc^+, 5.00 eV.[39, 48] Calculations were carried out using the Gaussian 16 software package (Revision A.03).[49]

Author Contributions

Samudra Amunugama: Methodology, syntheses, spectroscopic analysis, junction assembly, data analysis, writing of original draft.

Eyram Asempa: Formal analysis of theoretical calculations and writing of original draft for DFT calculations.

Elena Jakubikova: Formal analysis, supervision and writing of DFT section, funding acquisition for DFT portion.

Cláudio Verani: Overall conceptualization, formal analysis, data curation, project administration, supervision, and manuscript writing and revisions.

Conflicts of interest

There are no conflicts to declare.

Acknowledgements

The authors thankfully acknowledge financial support from the National Science Foundation through grants NSF-CHE1904584 and NSF-CHE-1500201 to CNV, including support to SA, and from the US Army Research Office under the contract W911NF-19-2-0194 to EJ including support to EAA. We also acknowledge the use of the NCSU High-Performance Computing Center.

Notes and references

1. (a) C. N. Verani, *Dalton Trans.*, 2018, **47**, 14153-14168; (b) D. C. Milan, A. Vezzoli, I. J. Planje and P. J. Low, *Dalton Trans.*, 2018, **47**, 14125-14138; (c) P. J. Low, *Dalton Trans.*, 2005, 2821-2824; (d) E. Coronado and M. Yamashita, *Dalton Trans.*, 2016, **45**, 16553-16555; (e) R. M. Metzger, *Chem. Rev.*, 2015, **115**, 5056-5115; (f) R. M. Metzger, *J. Mater. Chem.*, 2008, **18**, 4364-4396.
2. (a) C. Zhou, M. Deshpande, M. Reed, L. Jones and J. Tour, *Appl. Phys. Lett.*, 1997, **71**, 611-613; (b) P. T. Mathew and F. Fang, *Engineering*, 2018, **4**, 760-771.
3. J. Park, A. N. Pasupathy, J. I. Goldsmith, C. Chang, Y. Yaish, J. R. Petta, M. Rinkoski, J. P. Sethna, H. D. Abruña and P. L. McEuen, *Nature*, 2002, **417**, 722-725.
4. C. Li, W. Fan, D. A. Straus, B. Lei, S. Asano, D. Zhang, J. Han, M. Meyyappan and C. Zhou, *J. Am. Chem. Soc.*, 2004, **126**, 7750-7751.
5. E. A. Osorio, K. Moth-Poulsen, H. S. van der Zant, J. Paaske, P. Hedegård, K. Flensberg, J. Bendix and T. Bjørnholm, *Nano Lett.*, 2010, **10**, 105-110.
6. Q. Van Nguyen, U. Tefashe, P. Martin, M. L. Della Rocca, F. Lafolet, P. Lafarge, R. L. McCreery and J. C. Lacroix, *Adv. Electron. Mater.*, 2020, **6**, 1901416.
7. P. Sachan and P. C. Mondal, *Journal of Materials Chemistry C*, 2022, **10**, 14532-14541.
8. N. D. Paul, U. Rana, S. Goswami, T. K. Mondal and S. Goswami, *J. Am. Chem. Soc.*, 2012, **134**, 6520-6523.
9. Y. Lee, S. Yuan, A. Sanchez and L. Yu, *Chem. Commun.*, 2007, 247-249.
10. K. Seo, A. V. Konchenko, J. Lee, G. S. Bang and H. Lee, *J. Am. Chem. Soc.*, 2008, **130**, 2553-2559.
11. L. Scudiero, D. E. Barlow and K. Hipps, *J. Phys. Chem. B*, 2002, **106**, 996-1003.
12. A. Schmidt, N. Armstrong, C. Goeltner and K. Muellen, *J. Phys. Chem.*, 1994, **98**, 11780-11785.
13. X. Ding, J. Xue, S. Ding, C. Chen, X. Wang, X. Yu and W. Hu, *Angew. Chem. Int. Ed.*, 2022, **61**, e202208969.
14. C. Morari, L. Buimaga-Iarinca, I. Rungger, S. Sanvito, S. Melinte and G.-M. Rignanese, *Sci. Rep.*, 2016, **6**, 1-10.
15. D. Frath, V. Q. Nguyen, F. Lafolet, P. Martin and J.-C. Lacroix, *Chem. Commun.*, 2017, **53**, 10997-11000.
16. (a) R. M. Metzger, B. Chen, U. Höpfner, M. Lakshmikantham, D. Vuillaume, T. Kawai, X. Wu, H. Tachibana, T. V. Hughes and H. Sakurai, *J. Am. Chem. Soc.*, 1997, **119**, 10455-10466; (b) A. Aviram and M. A. Ratner, *Chem. Phys. Lett.*, 1974, **29**, 277-283.
17. S. Amunugama, E. Asempa, R. C. Tripathi, D. Wanniarachchi, H. Baydoun, P. Hoffmann, E. Jakubikova and C. N. Verani, *Dalton Trans.*, 2022.
18. (a) P. C. Mondal and A. K. Manna, *New J. Chem.*, 2016, **40**, 5775-5781; (b) C. Fu, C. Zhu, S. Wang, H. Liu, Y. Zhang, H. Guo, L. Tao and Y. Wei, *Polym. Chem.*, 2013, **4**, 264-267.
19. D. C. Wanniarachchi, M. J. Heeg and C. N. Verani, *Inorg. Chem.*, 2014, **53**, 3311-3319.
20. (a) M. Rupp, T. Auvray, E. Rousset, G. M. Mercier, V. Marvaud, D. G. Kurth and G. S. Hanan, *Inorg. Chem.*, 2019, **58**, 9127-9134; (b) K.-C. Cheung, P. Guo, M.-H. So, Z.-Y. Zhou, L. Y. S. Lee and K.-Y. Wong, *Inorg. Chem.*, 2012, **51**, 6468-6475; (c) M. I. Polson, E. A. Medlycott, G. S. Hanan, L. Mikelsons, N. J. Taylor, M. Watanabe, Y. Tanaka, F. Loiseau, R. Passalacqua and S. Campagna, *Chem. Eur. J.*, 2004, **10**, 3640-3648; (d) F. Barigelletti, B. Ventura, J. P. Collin, R. Kayhanian, P. Gaviña and J. P. Sauvage, *Eur.J.Inorg.Chem.*, 2000, **2000**, 113-119; (e) E. C. Constable, *Chem. Soc. Rev.*, 2007, **36**, 246-253.
21. (a) S. Bonnet, J.-P. Collin, N. Gruber, J.-P. Sauvage and E. R. Schofield, *Dalton Trans.*, 2003, 4654-4662; (b) L. N. Lameijer, T. G. Brevé, V. H. van Rixel, S. H. Askes, M. Siegler and S. Bonnet, *Chem. Eur. J.*, 2018, **24**, 2709-2717.
22. A. Gerli, J. Reedijk, M. T. Lakin and A. L. Spek, *Inorg. Chem.*, 1995, **34**, 1836-1843.
23. (a) A. Gelling, M. D. Olsen, K. G. Orrell, A. G. Osborne and V. Šik, *J. Chem. Soc., Dalton trans.*, 1998, 3479-3488; (b) A. M. CargilláThompson, *J. Chem. Soc., Dalton trans.*, 1992, 3467-3475; (c) W. K. Seok, S. W. Moon and M. Y. Kim, *Bull Korean Chem Soc*, 1998, **19**, 1207-1210; (d) W. J. Perez, C. H. Lake, R. F. See, L. M. Toomey, M. R. Churchill, K. J. Takeuchi, C. P. Radano, W. J. Boyko and C. A. Bessel, *J. Chem. Soc., Dalton trans.*, 1999, 2281-2292.
24. (a) S. Cerfontaine, L. Marcélis, B. Laramee-Milette, G. S. Hanan, F. Loiseau, J. De Winter, P. Gerbaux and B. Elias, *Inorg. Chem.*, 2018, **57**, 2639-2653; (b) G. S. Hanan, C. R.

Arana, J. M. Lehn, G. Baum and D. Fenske, *Chem. Eur. J.*, 1996, **2**, 1292-1302.
25. Z. N. Liu, C. X. He, H. J. Yin, S. W. Yu, J. B. Xu, J. W. Dong, Y. Liu, S. B. Xia and F. X. Cheng, *Eur.J.Inorg.Chem.*, 2021, **2021**, 482-491.
26. B. Siewert, M. Langerman, Y. Hontani, J. Kennis, V. Van Rixel, B. Limburg, M. Siegler, V. T. Saez, R. Kieltyka and S. Bonnet, *Chem. Commun.*, 2017, **53**, 11126-11129.
27. S. Das and B. Pradhan, *RSC Adv.*, 2015, **5**, 73726-73731.
28. (a) E. I. Solomon and A. B. P. Lever, *Inorganic Electronic Structure and Spectroscopy: Methodology*, Wiley, 2006; (b) T. A. White, S. Maji and S. Ott, *Dalton Trans.*, 2014, **43**, 15028-15037.
29. (a) L. Rayleigh and A. Pockels, *Nature*, 1891, **43**, 437; (b) A. Pockels, *Nature*, 1892, **46**, 418-419; (c) A. Pockels, *Nature*, 1893, **48**, 152-154; (d) A. Pockels, *Nature*, 1894, **50**, 223-224.
30. (a) H. E. Ries, *Nature*, 1979, **281**, 287-289; (b) R. Shakya, S. S. Hindo, L. Wu, M. M. Allard, M. J. Heeg, H. P. Hratchian, B. R. McGarvey, S. R. da Rocha and C. N. Verani, *Inorg. Chem.*, 2007, **46**, 9808-9818.
31. (a) F. D. Lesh, M. M. Allard, R. Shanmugam, L. M. Hryhorczuk, J. F. Endicott, H. B. Schlegel and C. N. Verani, *Inorg. Chem.*, 2011, **50**, 969-977; (b) Y. S. Obeng and A. J. Bard, *Langmuir*, 1991, **7**, 195-201.
32. (a) C. Akpo, E. Weber and J. Reiche, *New J. Chem.*, 2006, **30**, 1820-1833; (b) J.-F. Nierengarten, J.-F. Eckert, Y. Rio, M. del Pilar Carreon, J.-L. Gallani and D. Guillon, *J. Am. Chem. Soc.*, 2001, **123**, 9743-9748.
33. T. Hama, A. Kouchi, N. Watanabe, S. Enami, T. Shimoaka and T. Hasegawa, *J. Phys. Chem. B*, 2017, **121**, 11124-11131.
34. (a) Z. Tang, R. K. Hicks, R. J. Magyar, S. Tretiak, Y. Gao and H.-L. Wang, *Langmuir*, 2006, **22**, 8813-8820; (b) Z. Zhang, A. L. Verma, M. Yoneyama, K. Nakashima, K. Iriyama and Y. Ozaki, *Langmuir*, 1997, **13**, 4422-4427.
35. J. He, Q. Fu, S. Lindsay, J. W. Ciszek and J. M. Tour, *J. Am. Chem. Soc.*, 2006, **128**, 14828-14835.
36. L. D. Wickramasinghe, S. Mazumder, S. Gonawala, M. M. Perera, H. Baydoun, B. Thapa, L. Li, L. Xie, G. Mao and Z. Zhou, *Angew. Chem. Int. Ed.*, 2014, **53**, 14462-14467.
37. Q. Van Nguyen, F. Lafolet, P. Martin and J. C. Lacroix, *J. Phys. Chem. C*, 2018, **122**, 29069-29074.
38. A. I. Weeraratne, N. Rani, S. Amunugama, S. S. Perera, K. K. Kpogo, S. Mazumder and C. N. Verani, *J. Phys. Chem. C*, 2022, **126**, 21010-21021.
39. R. R. Gagne, C. A. Koval and G. C. Lisensky, *Inorg. Chem.*, 1980, **19**, 2854-2855.
40. (a) C. B. Smith, C. L. Raston and A. N. Sobolev, *Green Chem.*, 2005, **7**, 650-654; (b) J. Wang and G. S. Hanan, *Synlett*, 2005, **2005**, 1251-1254.
41. (a) A. D. Beck, *J. Chem. Phys*, 1993, **98**, 5648-5646; (b) A. D. Becke, *Physical review A*, 1988, **38**, 3098; (c) C. Lee, W. Yang and R. G. Parr, *Physical review B*, 1988, **37**, 785; (d) P. J. Stephens, F. J. Devlin, C. F. Chabalowski and M. J. Frisch, *The Journal of physical chemistry*, 1994, **98**, 11623-11627.
42. S. Grimme, *J. Comput. Chem.*, 2006, **27**, 1787-1799.
43. M. Kaupp, P. v. R. Schleyer, H. Stoll and H. Preuss, *J. Chem. Phys.*, 1991, **94**, 1360-1366.
44. R. Krishnan, J. S. Binkley, R. Seeger and J. A. Pople, *J. Chem. Phys.*, 1980, **72**, 650-654.
45. G. Scalmani and M. J. Frisch, *J. Chem. Phys.*, 2010, **132**, 114110.
46. P.-O. Löwdin, *Physical Review*, 1955, **97**, 1474.
47. (a) S. Gorelsky, *Journal*, 1997; (b) S. I. Gorelsky and A. Lever, *J Organomet Chem.*, 2001, **635**, 187-196.
48. H. M. Koepp, H. Wendt and H. Stkehlow, *Zeitschrift für Elektrochemie, Berichte der Bunsengesellschaft für physikalische Chemie*, 1960, **64**, 483-491.
49. M. Frisch, G. Trucks, H. Schlegel, G. Scuseria, M. Robb, J. Cheeseman, G. Scalmani, V. Barone, G. Petersson and H. Nakatsuji, *Inc., Wallingford CT*, 2016, **3**.